Dislocations near elastic instability in high-pressure body-centered-cubic magnesium

I. S. Winter, M. Poschmann, T. Tsuru, and D. C. Chrzan

Dislocations near elastic instability in high pressure body-centered cubic magnesium

I. S. Winter,[1] M. Poschmann,[1] T. Tsuru,[2] and D. C. Chrzan[1]

[1]*Department of Materials Science and Engineering,*

University of California, Berkeley, California 94720, USA

[2]*Nuclear Science and Engineering Center, Japan Atomic Energy Agency,*

2-4 Shirakata-Shirane, Tokai-mura, Ibaraki, Japan

Abstract

At high pressure, Mg is expected to transform to the body-centered cubic (BCC) phase. We use density functional theory to explore the structure of $\langle 111 \rangle$-type dislocation cores in BCC Mg as a function of pressure. As the pressure is reduced from the region of absolute stability for the BCC phase, the dislocation cores spread. When dislocation cores overlap the displacements of columns of atoms resemble the nanodisturbances observed in TiNb alloys known as Gum Metal. As the pressure is lowered further, these regions transform into the hexagonal close-packed (HCP) phase. The ideal tensile strength of BCC Mg is also computed as a function of pressure. Despite its low shear modulus, BCC Mg is predicted to be intrinsically brittle at absolute zero.

I. INTRODUCTION

Over a decade ago researchers at Toyota developed Gum Metal, a class of TiNb based metals that exhibit a wide variety of both novel and attractive properties.[1] These metals display an elastic limit of approximately $2-3\%$ at room temperature and 4% at 77 K, a yield strength of over 1 GPa, as well as Invar and Elinvar properties. In addition Gum Metal appears to fail at or near its ideal strength, a behavior that has been long thought impossible in a bulk material due to the prevalence of defect mediated plasticity.[2–4] Saito, *et al.* proposed three criteria for the emergence of the "super" properties of Gum Metal.[1] The material must have an average valence electron number (electron/atom ratio) of 4.24, a bond order of approximately 2.87 and a d-electron orbital energy level of roughly 2.45 eV.

Subsequent work on Gum Metal suggested that a more general connection can be made between the properties of Gum Metal and the proximity of a material to an elastic instability.[5–8] Gum Metals exist near the composition at which the body-centered cubic (BCC) phase becomes elastically unstable and transforms into the hexagonal close-packed (HCP) phase. The proximity to this lattice instability is apparent in the elastic constants. Specifically the reduced shear modulus, $C' = \frac{1}{2}(C_{11} - C_{12})$, goes to zero at the transition.[1,5] Based on continuum anisotropic linear elasticity theory (henceforth abbreviated as linear elasticity theory) an explanation for the apparent failure of Gum Metal near its ideal strength has been developed. As the elastic instability is approached the dislocations' core radii grow. For proper alloy compositions and sufficient dislocation densities (Gum Metal's "ideal" behavior emerges only after severe cold-working[1]) an applied stress can cause the spread dislocation cores to percolate, resulting in high shear stress regions, where plastic deformation via shear melting should be possible.[6]

This explanation for the appearance of Gum Metal like properties suggest that it might be possible to observe similar behavior in other alloy systems and at other types of lattice instability.[7] In fact, experimentally the BCC to face-centered cubic (FCC) instability has been exploited to produce a Fe-Ni-Co-Ti alloy with Gum Metal like properties.[9] As in the case of Gum Metal, the properties of this alloy are likely strongly influenced by the d-states of the component atoms. Experimentally, the only known examples of Gum Metals are based upon transition metals.

This suggests an interesting avenue of exploration. Can one develop a Gum Metal alloy

without the incorporation of transition metal elements? Such an alloy might be technologically interesting as it is likely to have a high specific strength. For example, a Mg based Gum Metal might be well suited for applications requiring a light weight structural alloy. In what follows, we consider the potential for a non-transition metal to display properties that have been linked to the "super" properties of TiNb based Gum Metals. We consider in detail the case of Mg under high pressure.

The BCC phase is elastically unstable in magnesium at ambient pressure,[16] but is predicted to be stabilized at high pressures.[10] This offers a useful model for examining the effect of an elastic instability on the dislocation core structure as pressure can be used to approach the instability. It is also a much simpler approach compared to varying the composition of a binary alloy to approach an elastic instability, as none of the complexities inherent to modeling a solid solution need to be considered.

We first calculate the relative stability of BCC Mg with respect to HCP as a function of pressure using density functional theory (DFT) and compare these results to those already in the literature. By determining the elastic constants for a range of pressures, we show that BCC Mg approaches an elastic instability associated with $C' \to 0$ and that this corresponds to a spreading of the dislocation core. Analysis of the dislocation core structure indicates that interactions between the spread cores take place. This leads, initially, to the formation of localized regions of shear (nanodisturbances) that are characteristic of Gum Metal,[42] and ultimately results in the nucleation of the HCP phase. Unlike Gum Metal, BCC magnesium is predicted to be intrinsically brittle, despite being highly elastically anisotropic and having a G/B value typically associated with ductility.

II.   THEORY

The calculation of elastic constants was done by following the method described by Sin'ko in which pressure terms are incorporated into the elastic constants.[18] The approach begins with writing the strain of the homogeneous body as a symmetric second-rank tensor, which is a function of the strain magnitude, γ, and is of the form

$$\epsilon_{ij} = s_{ij}\gamma + e_{ij}\gamma^2 + ... \tag{1}$$

Here s_{ij} and e_{ij} are the first- and second-order terms of the strain tensor. The elastic

constants can then be written as a function of both volume at a given pressure V, and the Lagrangian strain $\boldsymbol{\eta}$

$$\tilde{C}_{ijkl} = \frac{1}{V}\frac{\partial^2 E(V,\eta)}{\partial \eta_{ij}\partial \eta_{kl}} \tag{2a}$$

$$\eta_{ij} = \epsilon_{ij} + \frac{1}{2}\epsilon_{ik}\epsilon_{kj}. \tag{2b}$$

It should be noted that the Einstein summation convention is used throughout this paper. Taking the Taylor series expansion of the strain energy with respect to the strain magnitude results in

$$\sum_{\alpha,\beta}\xi_\alpha\xi_\beta\tilde{C}_{\alpha\beta}s_\alpha s_\beta = 2P(V)\sum_\alpha(2-\xi_\alpha)e_\alpha + P(V)\sum_\alpha\xi_\alpha s_\alpha^2 + \frac{1}{V}\frac{\partial^2 E(V,\gamma)}{\partial\gamma^2}|_{\gamma=0}. \tag{3}$$

The above equation is written in Voigt notation with the indices ranging from 1 to 6 and $\xi_\alpha = 1$ if $\alpha \le 3$ and $\xi_\alpha = 2$ if $\alpha > 3$. Tsuchiya and Kawamura found that by selecting the strain configurations appropriately, the cubic elastic constants under pressure $(\tilde{C}_{ij})$ can be calculated from equation 3 using the following equations[20]

$$\tilde{C}_{11} = \frac{1}{V}\frac{\partial^2 E(V,\hat{\boldsymbol{\epsilon}}_4)}{\partial\gamma^2}|_{\gamma=0} \tag{4}$$

$$\tilde{C}_{44} = -\frac{P}{2} + \frac{1}{12V}\frac{\partial^2 E(V,\hat{\boldsymbol{\epsilon}}_5)}{\partial\gamma^2}|_{\gamma=0} \tag{5}$$

$$\tilde{C}_{11} - \tilde{C}_{12} = -P + \frac{1}{2V}\frac{\partial^2 E(V,\hat{\boldsymbol{\epsilon}}_6)}{\partial\gamma^2}|_{\gamma=0}. \tag{6}$$

Here the strain tensors $\hat{\boldsymbol{\epsilon}}_4$, $\hat{\boldsymbol{\epsilon}}_5$, and $\hat{\boldsymbol{\epsilon}}_6$ are defined as follows

4

$$\hat{\epsilon}_4 = \begin{pmatrix} \gamma & 0 & 0 \\ 0 & 0 & 0 \\ 0 & 0 & 0 \end{pmatrix} \tag{7a}$$

$$\hat{\epsilon}_5 = \begin{pmatrix} 0 & \gamma & \gamma \\ \gamma & 0 & \gamma \\ \gamma & \gamma & 0 \end{pmatrix} \tag{7b}$$

$$\hat{\epsilon}_6 = \begin{pmatrix} \gamma & 0 & 0 \\ 0 & -\gamma & 0 \\ 0 & 0 & 0 \end{pmatrix}. \tag{7c}$$

Ideal tensile strength calculations can be performed to determine if a material is intrinsically brittle or ductile.[21,22] The eigenvalues of the symmetrized Wallace tensor,[13,23] λ_{ijkl}, govern the elastic stability of a material following

$$\lambda_{ijkl}\delta\epsilon_{ij}\delta\epsilon_{kl} \geq 0. \tag{8}$$

In the case of a uniaxial load, σ, on a BCC material applied along $\langle 001 \rangle$ the elastic stability criteria are

$$(C_{33} + \sigma)(C_{11} + C_{22}) > 2\left(C_{13} - \frac{\sigma}{2}\right)^2 \tag{9a}$$

$$C_{11} - C_{22} > 0 \tag{9b}$$

$$C_{66} > 0 \tag{9c}$$

$$C_{44} + \frac{\sigma}{2} > 0. \tag{9d}$$

The failure of conditions 9b-9d correspond to a shear instability (intrinsic ductility) while condition 9a results in cleavage.[13] The elastic constants are of a body-centered tetragonal (BCT) Bravais lattice due to an uniaxial load being applied to the BCC crystal. The strain states used to calculate the six elastic constants of a BCT lattice under pressure are shown in the appendix (VIII B).

The elastic constants can be used to define a size for a dislocation core. By defining the dislocation core as the region for which the stress predicted by linear elasticity theory is greater than the ideal strength, an approximation for the region in which linear elasticity

theory is no longer valid is obtained.[6,7] Since symmetry often links the ideal strength to the elastic constants, this definition allows for the dislocation core radius to be written in terms of the elastic constants. In the case of a BCC metal the dislocation core radius can be expressed as

$$r_{core} = \frac{bK}{2\pi f G_{\langle 111 \rangle}}. \tag{10}$$

Here b is the Burgers vector, K, the elastic modulus governing the dislocation line tension, $G_{\langle 111 \rangle}$, the shear modulus along the $\langle 111 \rangle$ direction (that for BCC is independent of slip plane), and, f, a constant equal to approximately $1/9$ in the case of BCC.[7] K and $G_{\langle 111 \rangle}$ can be expressed as

$$K = \sqrt{(C_{11} - C_{12})C_{44}} \sqrt{\frac{2C_{11}^2 + 2C_{11}C_{12} - 4C_{12}^2 + 13C_{11}C_{44} - 7C_{12}C_{44} + 2C_{44}^2}{3(C_{11} - C_{12} + 4C_{44})(C_{11} + C_{12} + 2C_{44})}} \tag{11}$$

$$G_{\langle 111 \rangle} = \frac{3C_{44}(C_{11} - C_{12})}{C_{11} - C_{12} + 4C_{44}}. \tag{12}$$

The result of equation 10 is that the dislocation core radius is inversely proportional to $\sqrt{C_{11} - C_{12}}$. It has been argued that in the case of Gum Metal, due to its small reduced shear modulus the application of an applied stress can cause the dislocation core region to percolate resulting in paths of shear melting.[6,36]

DFT can be used to compute dislocation core structures using periodic supercells of $\langle 111 \rangle$ oriented screw dislocations following the approach of Daw.[37] This approach assumes that the distortion tensor can be written as a Fourier series

$$\Delta_{jk}(\mathbf{r}) = \sum_{\mathbf{G}} \tilde{\Delta}_{jk}(\mathbf{G})e^{i\mathbf{G}\cdot\mathbf{r}} \tag{13}$$

where $\tilde{\Delta}_{jk}(\mathbf{G})$ is a component of the distortion in reciprocal space and $\mathbf{G}$ corresponds to a reciprocal lattice vector. The elastic energy is written as

$$W_c = \frac{1}{2} \int_{cell} dv C_{jklm} \Delta_{jk} \Delta_{lm} = \frac{1}{2} \Omega_c C_{jklm} \sum_{\mathbf{G}} \tilde{\Delta}_{jk} \tilde{\Delta}_{lm}^*. \tag{14}$$

Here $\tilde{\Delta}_{lm}^*$ is the complex conjugate of $\tilde{\Delta}_{lm}$, C_{jklm} is the elastic tensor, and Ω_c is the volume of the cell. The equilibrium distortion tensor is determined by minimizing W_c with respect

to the distortion components subject to the constraints imposed by the dislocations. The distortion is then integrated to produce the initial displacements for our unit cells. In our numerical work the core radius was chosen to be $b/4$.

The distortion in the cell vectors due to the introduction of the dislocation quadrupole was determined as done by Lehto and Öberg.[32] Analysis of the dislocation core structure was carried out using differential displacement maps (DD) as developed by Vitek, *et al.*.[33] In these maps, the magnitude of an arrow between two nearest neighbor (NN) atoms shows the relative displacement, normal to the page, between the two atoms as a result of the dislocation. The arrows are scaled such that an arrow connecting NN represents a displacement of $b/3$. For a $\langle 111 \rangle$-type screw dislocation in BCC a full dislocation is symbolized in a DD map as a circuit which sums to b (e. g. a triangle of NN atoms connected by arrows of magnitude $b/3$ and pointing clockwise). The Nye tensor was calculated using the approach outlined by Hartley and Mishin.[30,31]

III. COMPUTATIONAL DETAILS

The relative phase stability of BCC and HCP Mg, the elastic constants, dislocation core structure, and ideal tensile strength calculations were all performed using the projector augmented wave method (PAW) as implemented in the Vienna Ab Initio Simulation Package (VASP).[11,12] For the exchange-correlation functional the Perdew, Becke, and Ernzerhof (PBE) Generalized Gradient Approximation was employed.[15] Both the 2p as well as the 3s states were considered as valence electrons. Phase stability calculations using PAW were conducted using primitive unit cells. A plane-wave cutoff of 580 eV was used with a first-order Methfessel-Paxton scheme and a smearing parameter of 0.1 eV. The convergence condition for electronic and ionic relaxations were set to 1×10^{-6} eV and 0.005 eV/Å respectively. These values were used for all other PAW calculations, unless otherwise stated. For BCC a $21 \times 21 \times 21$ Monkhorst-Pack grid was used, while for HCP a $21 \times 21 \times 13$ Γ-centered grid was implemented instead. The elastic constants calculations used a $25 \times 25 \times 25$ Monkhorst-Pack grid with a conventional BCC unit cell. Electronic relaxations for elastic constants calculations were set to 1×10^{-10} eV. A 135 atom BCC unit cell was used with $2 \times 1 \times 8$ Γ-centered grid for dislocation core calculations.

Ideal strength calculations[21,22] were performed by applying a fixed strain along the [001]

7

direction, as this is considered the weakest direction under tension for BCC metals,[24,25] and varying the strain along [100] and [010] to achieve the proper stress state. Relaxations were performed until all components of the stress tensor other than σ_{33} were less than 0.05 GPa. Brillouin zone integrations were performed using a $29 \times 29 \times 29$ Monkhorst-Pack grid. The intrinsic ductility of the material was tested by allowing the unit cell to relax along a tetragonal path. The symmetrized Wallace tensor was evaluated by calculating the BCT elastic constants using the same input parameters as for the cubic elastic constants described above. The strain states for the BCT elastic constants are defined in equation 15 of the appendix (VIII B).

The relative phase stability as well as the density-of-states as a function of pressure were also performed using the full-potential linearized augmented plane wave (FP-LAPW) method as implemented in the code Elk.[14] Convergence testing was conducted with respect to the muffin-tin radius, k-point sampling, and plane-wave cutoffs. A total energy convergence criterion of 3.0×10^{-8} Ha was used. A smoothing of 0.001 Ha was used for the Dirac delta function.

IV. RESULTS

The phase stability of BCC and HCP structures was considered using both FP-LAPW and PAW. Both methods result in a general agreement for the behavior of the energy of the BCC phase in magnesium as a function of pressure as shown in figure 1. This leads to the conclusion that the PAW method, while not an all-electron method, models the given system reasonably well, and is suitable for our calculations. The BCC-HCP transition volume and pressure, computed with PAW, are in general agreement with previous work conducted using the linear muffin-tin orbitals method (LMTO) as shown in table 1. The current work's values for transition volume and pressure differ from that of reference[10] by 0.8% and 7% respectively. The partial density of states calculated using FP-LAPW shown in figure 1d demonstrates that the occupation of the d-states are negligible at least for volumes $V = 0.6V_0$ and higher. Calculations of the density of states, figure 2, at volumes between $0.6V_0$ and $0.7V_0$ using FP-LAPW show that the elastic instability does not appear to be related to the Fermi level approaching a van Hove singularity, which is associated with the low shear modulus, C_{44}, seen in V, Nb, and Ta.[26–28] Using the common tangent

construction figure 1 indicates that the two phase region does not extend far beyond the transition pressure, which is calculated to be approximately 50 GPa and corresponds to a volume of $0.6V_0$. However, the BCC phase remains elastically stable for volumes approaching V_0 as shown in figure 3 and table II.
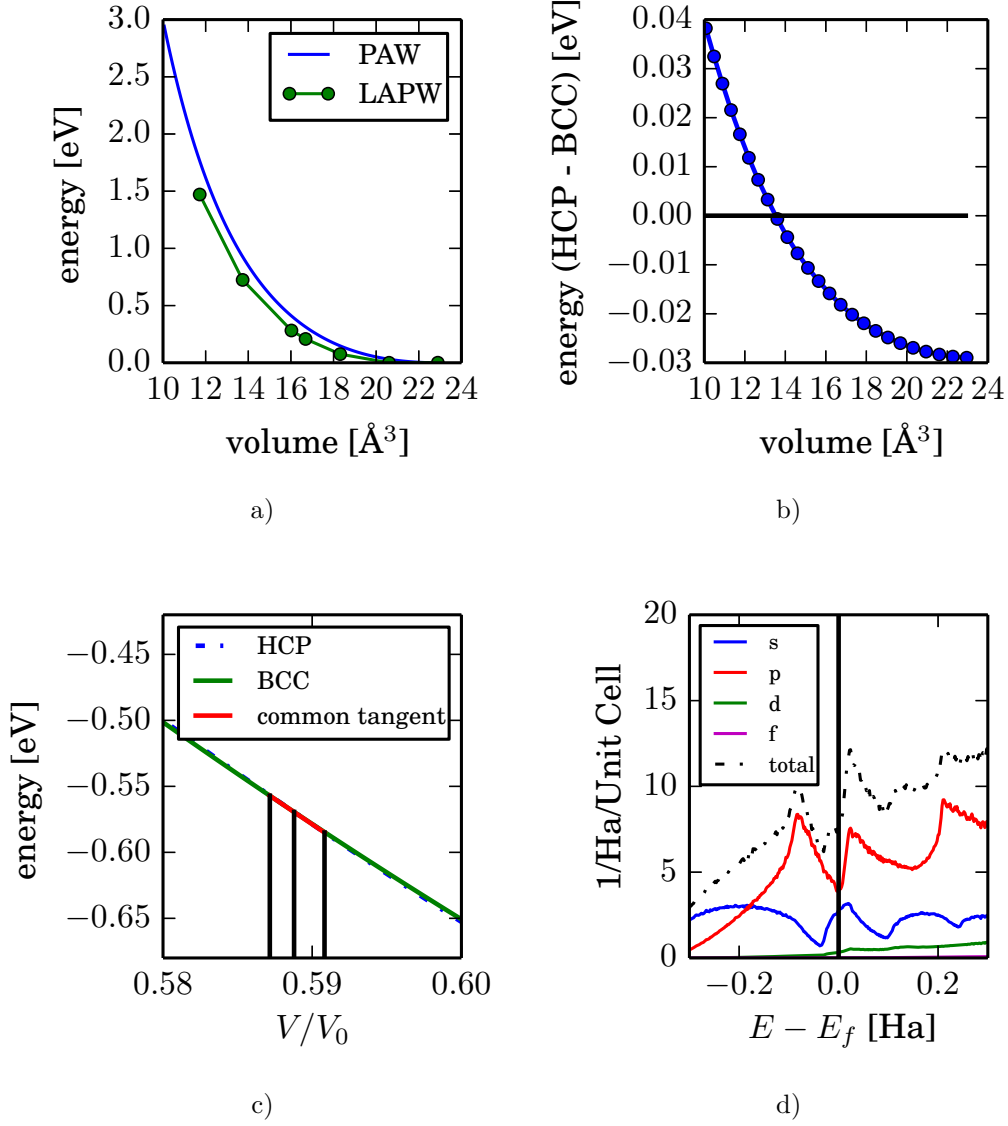

FIG. 1. Comparison of the total energy of the BCC phase using both the FP-LAPW and PAW methods in 1a. Figure 1b shows a plot of the relative stability of BCC with respect to HCP as a function of volume. The BCC phase becomes stable at roughly half of the volume corresponding to ambient pressure and volume. Common tangent construction for BCC and HCP as a function of volume ratio is illustrated in figure 1c. The partial density of states (DOS) for magnesium at $V = 0.6V_0$ is shown in figure 1d.
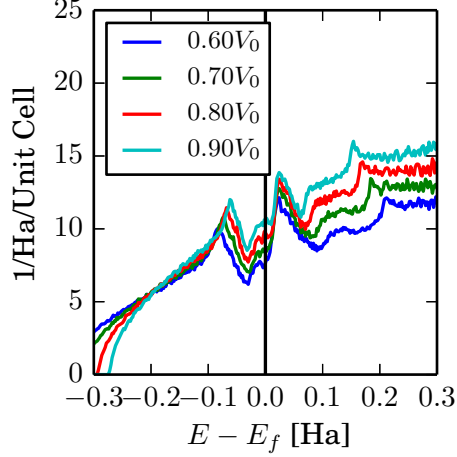
FIG. 2. Total density of states for volumes between $0.60V_0$ and $0.90V_0$ using FP-LAPW.

TABLE I. BCC-HCP transformation data. V_0 corresponds to the volume of HCP magnesium under no applied pressure.

V_0 (HCP) [Å^3]	V_{trans} [Å^3]	P_{trans} [GPa]	Ref.
23.0	13.5	53.8	current work
23.2	13	50	[10]
—	—	50 ± 6	[19]

The elastic stability of the BCC phase was computed and compared to previous work (figure 3a). As ambient pressure is approached the BCC lattice becomes elastically unstable. Based on the arguments given above this should result in an increase in the dislocation core radii. The dislocation core radius normalized by the burgers vector as calculated from elasticity theory is shown in figure 3b. For volumes $0.6V_0 - 0.9V_0$ the core radius is large compared to Gum Metal, but also increases as the elastic instability is neared. For comparison the dislocation core radius of tungsten, a nearly elastically isotropic crystal, was estimated to be 1.45.[6]

As shown in table II, the dislocation core radii of Gum Metal and the Ti$_3$Nb Gum Metal approximate are relatively close to the that of tungsten. The dislocation core radius of

10
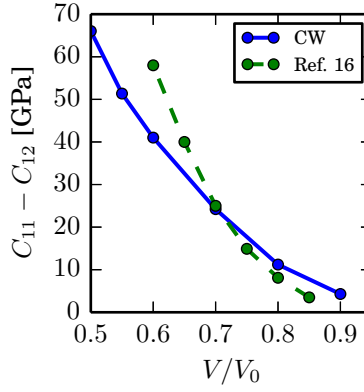
a)
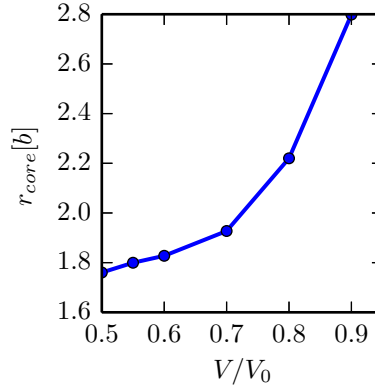
b)

FIG. 3. Figure 3a compares LMTO results from reference[16] with PAW (Current Work). Figure 3b shows the change in the ratio between the dislocation core radius, r_{core}, and magnitude of the Burgers vector, b. Lowering the pressure of Mg appears to cause $C_{11} - C_{12} \to 0$, leading the BCC phase to become elastically unstable.

$Ti_{80}V_{20}$, however, is 2.42. Ti_3Nb contains 4.25 valence electrons per atom (e/a), while $Ti_{80}V_{20}$ has 4.20 e/a. Near an elastic instability small fluctuations in composition (changes in e/a) can have a dramatic impact on the dislocation core radius, leading to the potential for different mechanisms for plasticity in different regions of the material. Substituting pressure for composition this same behavior is apparent. Comparing figures 3a and 3b, as $C_{11} - C_{12}$ approaches zero the dislocation core radius increases.

Dislocations core structures were computed as described in section III. A quadrupolar configuration for the dislocations was selected as this has been shown to be energetically

TABLE II. Comparison of relative core radii and elastic constants for various Gum Metal approximants. All elastic constants are in units of GPa.

Material	C_{11}	C_{12}	C_{44}	C'	r_{core}/b
$Ti_{80}V_{20}$ (Theory)[6]	139	131	47	4	2.42
Ti_3Nb (Theory)[38]	149	111	37.5	18.7	1.51
Ti–36Nb–2Ta–3Zr–0.3O (wt.%)[39]	125	93	28	16	1.49
Mg ($V = 0.6V_0$)	207	178	124	14.5	1.83
Mg ($V = 0.7V_0$)	137	112	85.5	12.5	1.93
Mg ($V = 0.8V_0$)	84.2	76.1	59.9	4.05	2.51

favorable to a conventional dipole stacking.[32] Figure 4 illustrates the expansion of the dislocation cores in the quadrupolar configuration as the volume increases from 65% to 80% of the ambient volume coinciding with the drop in the reduced shear modulus as seen in figure 3. The dislocation densities of the screw quadrupolar configuration at $0.65V_0$, $0.70V_0$, and $0.80V_0$ is 2.66×10^{17} m^{-2}, 2.53×10^{17} m^{-2}, and 2.32×10^{17} m^{-2} respectively. It should be noted that the lateral displacements of atoms on the (111) plane are included in this plot. The large displacements shown in the DD map for the two larger volumes are indicative of the phase transformation of BCC to HCP as illustrated in figure 4 by adaptive common neighbor analysis (a-CNA)[40] as implemented in the open visualization tool (OVITO).[41] This is especially evident for $0.8V_0$, where the dislocations appear to have initiated the transformation of almost the entire supercell into HCP (red atoms). Considering that this material has been designed specifically such that C' approaches zero, the appearance of HCP in the dislocation core is understandable. The $0.65V_0$ dislocation cores display an approximant three-fold symmetry near the center of the dislocation similar to those found by Vitek, et $al.$ for Fe.[33] These correspond to the three {112} type planes intersecting the dislocation cores. Interestingly, the Burgers path, which connects the BCC to HCP phase[34] consists of a near $\{11\bar{2}\}\langle111\rangle$ shear coupled with a softening of N-point acoustic phonon mode.[35]

Figure 5 depicts the projection of a screw dislocation quadrupole with all atoms projected onto the (111) plane in order to better visualize any lateral shifts resulting from the dislocations. The large degree of lateral displacements for both volumes is associated with a highly
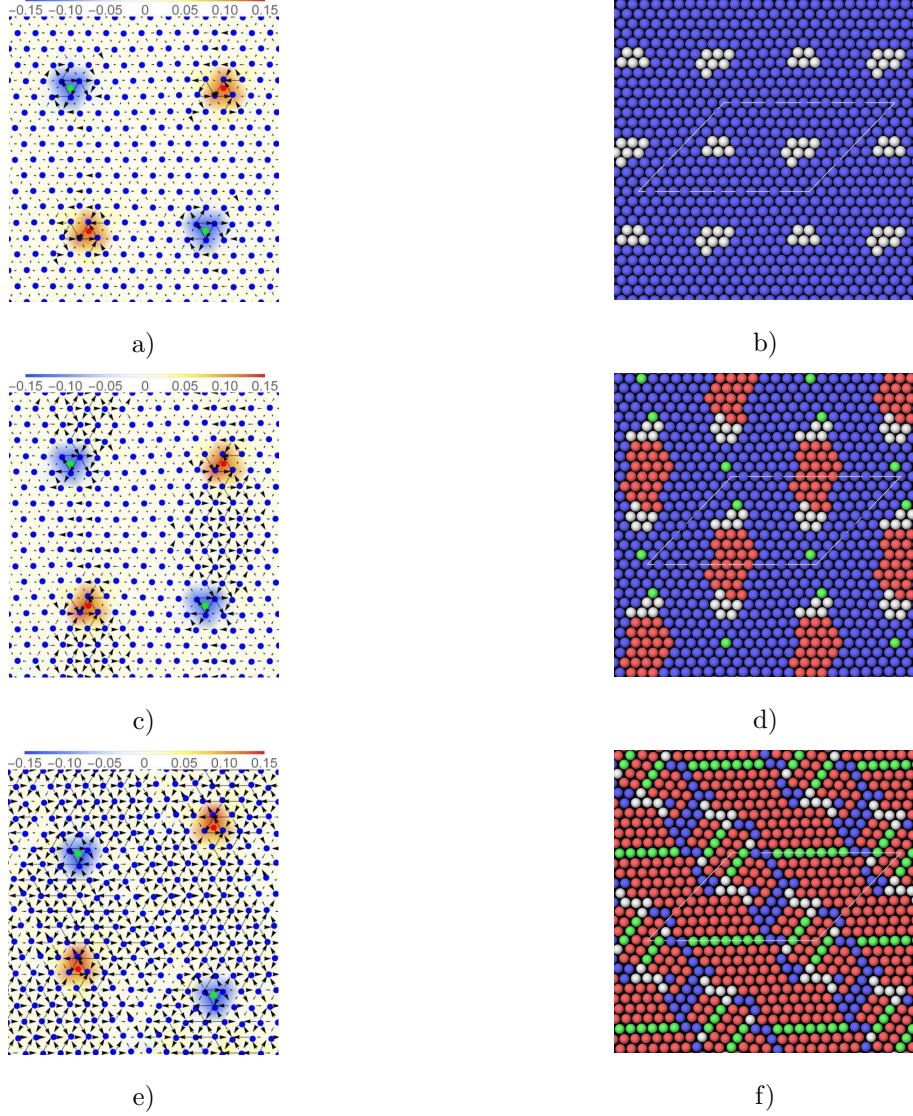
FIG. 4. Comparison of relaxed $\langle 111 \rangle$ screw dislocations in a quadrupolar configuration for BCC magnesium at $0.65V_0$, $0.7V_0$, and $0.8V_0$ (figures a, c, and e respectively). Figures b, d, and f show atoms colored using CNA for $0.65V_0$, $0.7V_0$, and $0.8V_0$. Red atoms are HCP, blue atoms correspond to BCC, green FCC and white are unclassified.

anisotropic material based on a comparison to TiV dislocation cores.[6] In figure 5a localized regions of shear can be seen reminiscent of nanodisturbances (defined as a dipole of partial dislocations with Burgers vectors not corresponding to the crystal) seen in Gum Metal[42] as well as TiV Gum Metal approximants.[6] In order to determine if the lateral displacements in the atoms claimed to be nanodisturbances in figure 5 are associated with edge dislocations, the edge component of the Nye tensor was plotted for the dislocation quadrupolar

configuration. From figure 6 no edge character is apparent for either $0.65V_0$ or $0.7V_0$ BCC Mg. However, in the case of $0.8V_0$ there is a direct correspondence between the regions of possible edge character outlined in figure 5 and the regions of high edge character in figure 6, both of which are outlined by green circles in the two figures.
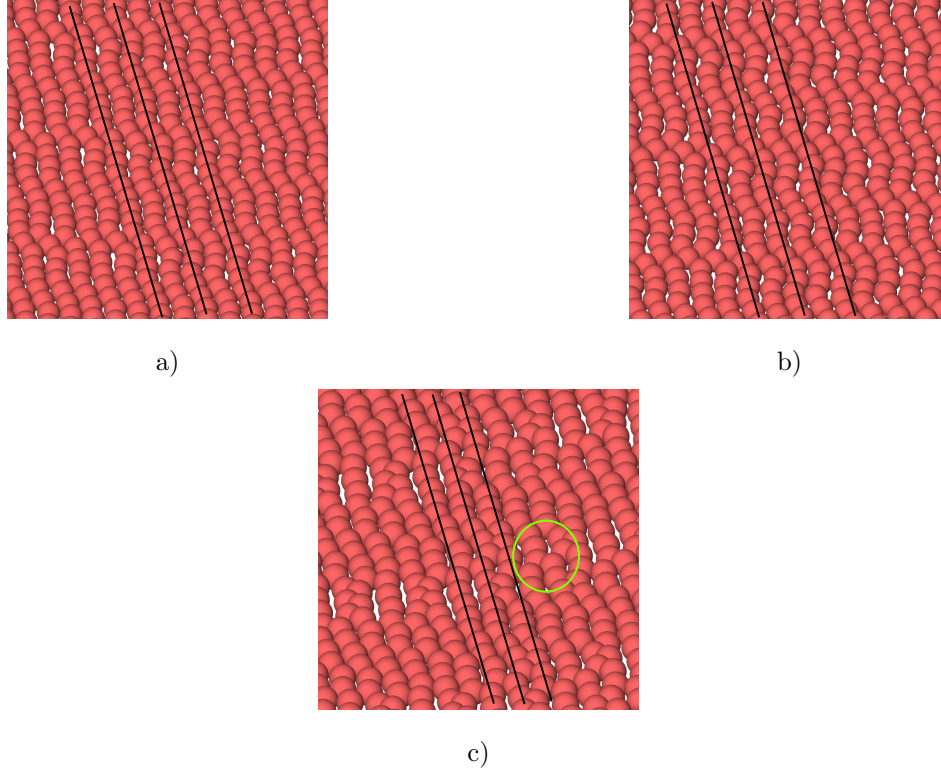

FIG. 5. Projection of relaxed $\langle 111 \rangle$ screw dislocations in a quadrupolar configuration onto the (111) plane for BCC magnesium at $0.65V_0$, $0.7V_0$, and $0.8V_0$ (figures a, b, and c respectively). In figure 5c, a region of suspected edge character is highlighted by the green circle.

The pressure dependence of the ideal tensile strength was computed in order to explore the intrinsic brittle/ductile behavior of BCC magnesium. For the material to be intrinsically ductile it must fail under a uniaxial tensile load via a shear instability instead of via cleavage (intrinsically brittle). A failure of condition 9a is a consequence of a material being intrinsically brittle, as the eigenvector associated with this condition does not result in any shearing of the crystal. A uniaxial stress is applied along $\boldsymbol{c}$ and relaxations are performed under the constraint that the lattice remains BCT. The elastic stability at each strain is then determined from the eigenvalues of the symmetric Wallace tensor following equations 9a-9d.
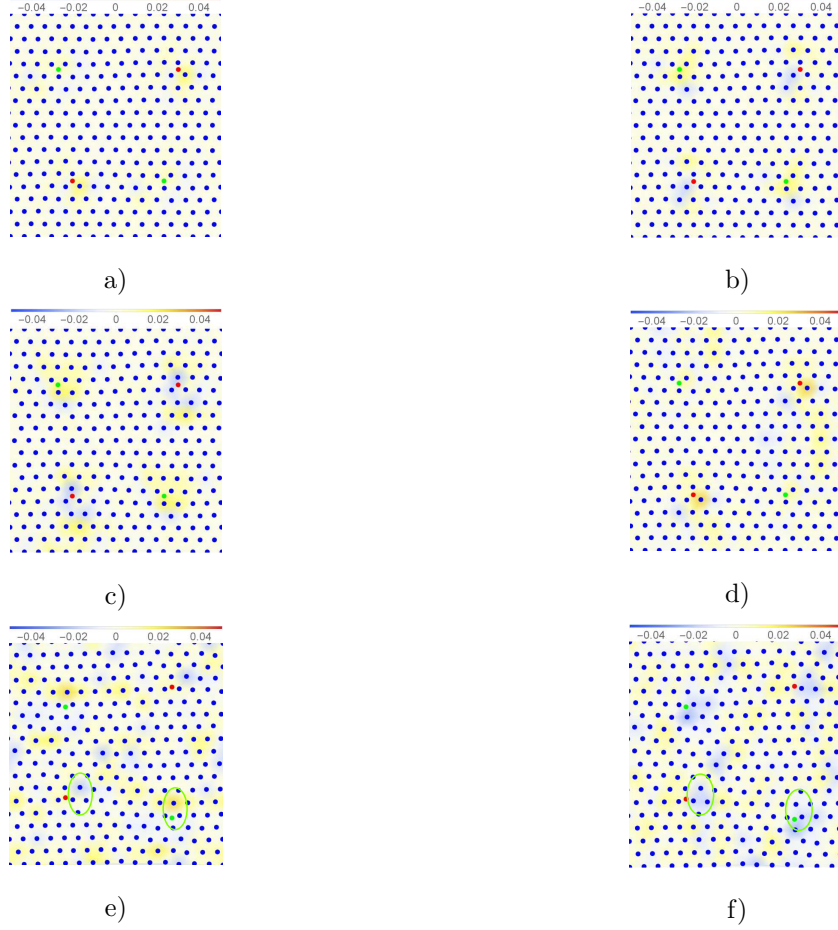
14

FIG. 6. Comparison of relaxed $\langle 111 \rangle$ screw dislocations in a quadrupolar configuration for BCC magnesium at $0.65V_0$, $0.7V_0$, and $0.8V_0$ (first, second and third rows respectively). Coloring is done using the edge components, α_{13} and α_{23}, of the Nye tensor for the left and right columns respectively. The atom positions of plots show the lateral shifts resulting from the dislocations. The green circles identify regions that correspond to the regions of edge character in figure 5.

BCC magnesium at both $0.65V_0$ and $0.7V_0$ is indicated to be intrinsically brittle as shown in figure 7. Both volumes show an elastic instability due to cleavage at approximately $2\% - 4\%$ strain. The initial instability due to cleavage is relatively shallow, meaning that slight differences in the elastic constants could cause a change in behavior. This was tested by varying the smearing parameter. The elastic constants were run for smearings of 0.05 eV, 0.1, 0.2, and 0.3 eV. For all values the cause of elastic instability was found to be the same (cleavage).
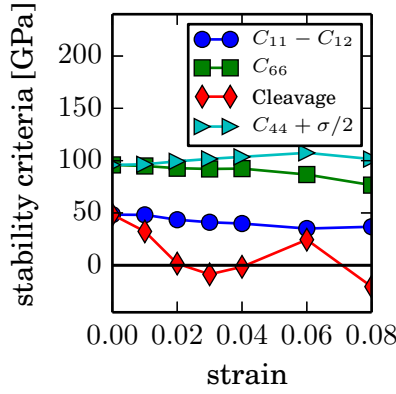
a)
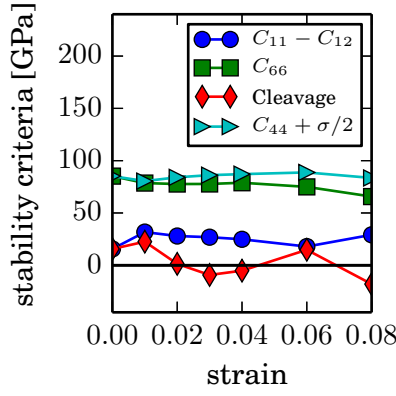
b)

FIG. 7. The eigenvalues of the symmetric Wallace tensor, which correspond to the elastic stability criteria of a crystal under an uniaxial load are shown for $0.65V_0$ and $0.7V_0$ in figures 7a and 7b respectively. Both volumes show an elastic instability at $2\% - 4\%$ that is a result of cleavage.

The formation of an elastic instability at such small strains $2\% - 4\%$ is an unusual feature. Examining the change in the density of states as shown for the two volume $0.65V_0$ and $0.70V_0$ in figures 8b and 8c, there does appear to be a large shift in the DOS for both volumes at the approximate energy range -2 eV to -1 eV. The application of an uniaxial load changes the point group of the crystal from O_h to D_{4h}. This causes the group of the wave vector along $Z_2 \rightarrow P$ to change from C_{3v} to C_{1h}. As C_{1h} has no 2 dimensional irreducible representation the band splits as shown in figure 8a. The same band splits at Z as a result of a change in the group of the wave vector from O_h to D_{4h}. As shown in figure 8a the splitting of this band appears to be associated with an overall increase in the energy of the occupied states
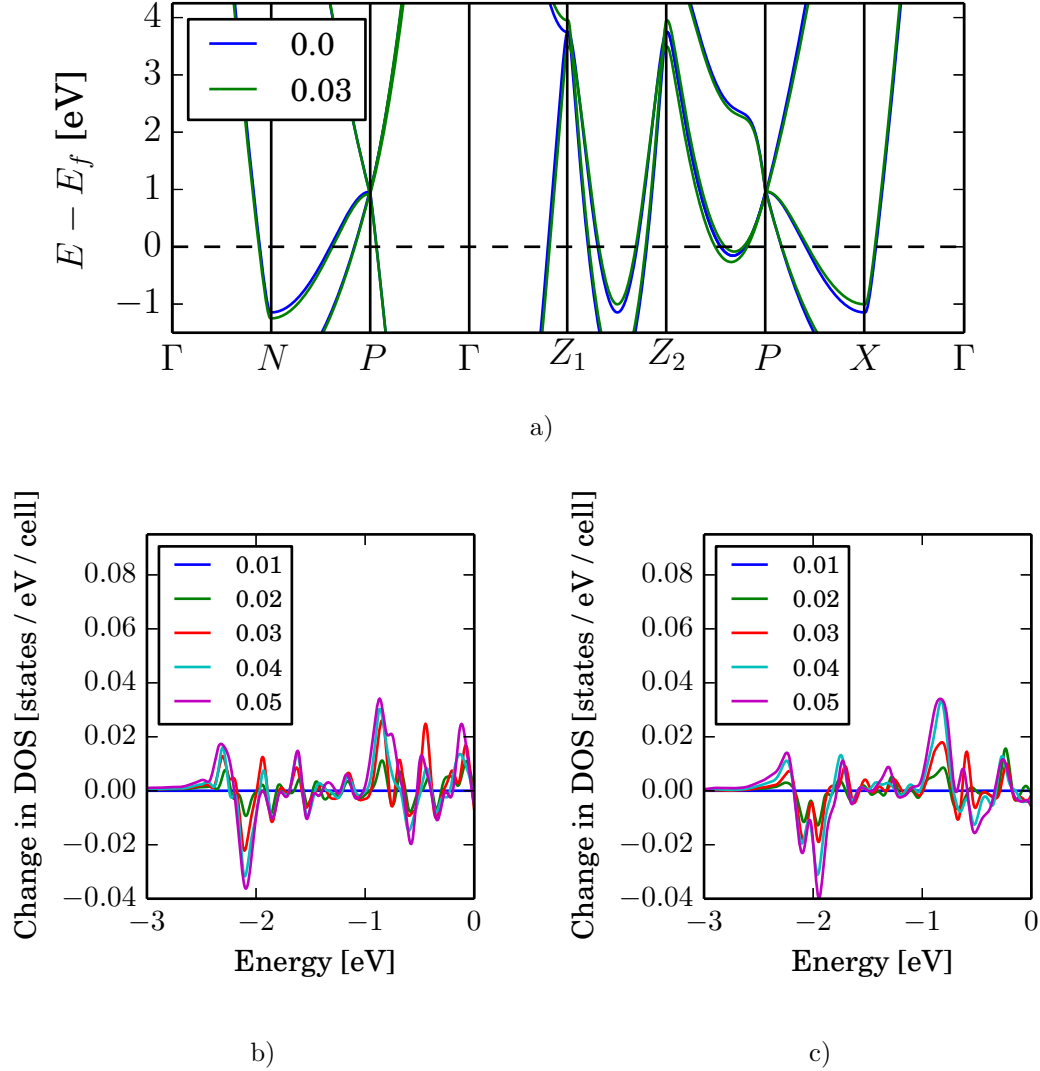
16

FIG. 8. The band structure of $0.65V_0$ is shown with 3% applied strain and no strain (8a). The band structure of $0.70V_0$ resembles very closely that of $0.65V_0$. The change in the density of states with strain is shown in figures 8b and 8c. The high symmetry points are those of a body-centered tetragonal lattice:[43] $\Gamma = [000]$, $N = \frac{1}{2}[100]$, $P = \frac{1}{4}[111]$, $Z_1 = \frac{1}{2}[11\bar{1}]$, $Z_2 = \frac{1}{2}[111]$, and $X = \frac{1}{2}[001]$. Z_1 and Z_2 are symmetrically equivalent k-vectors in reciprocal space both corresponding to the high symmetry point, Z.

$(Z_1 \rightarrow Z_2)$. Interestingly, The two-fold degeneracy of the band at Z is consistent with that of a d-band.[44] There does appear to be some d-like character near and above the Fermi level as shown in figure 1d, although it is much smaller than the s- and p-states. It does entertain the idea though that the d-electrons, while playing no significant role in bonding of the cubic

17

crystal, could be involved enough in the strained state to contribute to the material failing in cleavage.

V. DISCUSSION

BCC magnesium draws many parallels to Gum Metal. Linear elasticity theory shows that a reduction in the reduced shear modulus with decreasing pressure is associated with an expansion in the dislocation core radius as well as an increase in the elastic anisotropy of the crystal. The strain field due to a screw dislocation contains more than one non-zero component for a highly anisotropic crystal leading to large lateral displacements. Dislocation core structure calculations show that as the pressure is reduced lateral displacements become more pronounced to the point where nanodisturbances appear. Associated with this is the formation of HCP via the Burgers path starting at the dislocation core. These observations are all consistent with a previously stated explanation for ideal slip in a bulk material.[6] Heavily cold-working a material near an elastic instability results in a high density of dislocations, which exhibit large core structures. An applied stress can cause the dislocation core region to overlap, resulting in highly stressed regions in which shear bands associated with the Burgers path can form.

Unlike Gum Metal, BCC magnesium appears to be intrinsically brittle. With this noted, the behavior of BCC Mg is especially intriguing considering that the anisotropic Pugh criterion,[45] $B/G_{\langle 111 \rangle}$, for $0.7V_0$ BCC Mg is approximately 6.89, suggesting it is ductile. For comparison niobium, vanadium, and tantalum (all intrinsically ductile BCC metals) are approximately 7.9, 5.5, and 3.3 respectively. As all calculations have been conducted at 0 K there is a possibility that a brittle to ductile transition can occur within the BCC phase.

Assuming that a material must (1) be near an elastic instability and (2) be intrinsically ductile for its plasticity to be governed by the ideal shear strength (ISS), the case for BCC magnesium appears to be in doubt. Condition (2) appears obvious for a perfectly crystalline material. However, bulk materials will always contain defects and if the theoretical studies on materials governed by ISS are to believed it is only at enormous defect densities that the ISS will begin to govern the yield strength. The complex stress fields associated with a high dislocation density bring into question whether a material must be intrinsically ductile to have its plasticity governed by the ISS.

VI. CONCLUSION

The properties of BCC Mg nearing its elastic instability have been investigated using DFT. Calculations of the elastic constants at pressure show that the reduced shear modulus of the BCC phase approaches zero with decreasing pressure, resulting in a highly anisotropic material for volumes $0.60V_0$ - $0.80V_0$. Dislocation core calculations show the formation of nanodisturbances between screw dislocations, which have been experimentally observed in Gum Metal. The formation of nanodisturbances is shown to coincide with the appearance of the HCP phase at or near the dislocation core. Ideal tensile strength calculations indicate that, unlike Gum Metal, BCC magnesium is intrinsically brittle. The lack of d-states in bonding for BCC magnesium leads to the suggestion that an intrinsically ductile material near an elastic instability could behave like Gum Metal.

VII. ACKNOWLEDGMENTS

VIII. APPENDIX

A. Dislocation Core Structure

The full dislocation core structure calculations can be seen for both the $0.7V_0$ as well as $0.8V_0$ samples of BCC magnesium. The figures depict a 2×2 supercell created from the original 135 atom cell, which consists of two dislocations. Relatively large magnitudes of the Nye tensor components along the edges of the supercell are a result of boundary effects in calculating the Nye tensor.
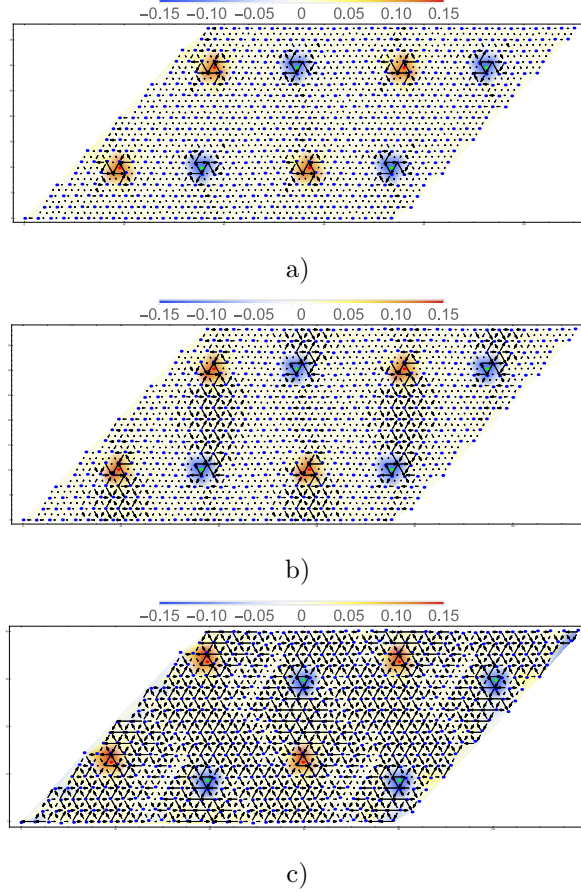
FIG. 9. Comparison of relaxed $\langle 111 \rangle$ screw dislocations in a quadrupolar configuration for BCC magnesium at $0.7V_0$ and $0.8V_0$ showing the entire supercell (figures a and b respectively). Coloring is done using the screw component of the Nye tensor.

B. Tetragonal Elastic Constants under Pressure

For a tetragonal lattice the elastic constants at pressure can be calculated using the following six strains defined as $\hat{\epsilon}_1^{tetr}$, $\hat{\epsilon}_2^{tetr}$, $\hat{\epsilon}_3^{tetr}$, $\hat{\epsilon}_4^{tetr}$, $\hat{\epsilon}_5^{tetr}$, and $\hat{\epsilon}_6^{tetr}$, which are represented in tensor form as

$$\hat{\epsilon}_1^{tetr} = \begin{pmatrix} \gamma & 0 & 0 \\ 0 & 0 & 0 \\ 0 & 0 & 0 \end{pmatrix} \tag{15a}$$

$$\hat{\epsilon}_2^{tetr} = \begin{pmatrix} 0 & 0 & 0 \\ 0 & 0 & 0 \\ 0 & 0 & \gamma \end{pmatrix} \tag{15b}$$

$$\hat{\epsilon}_3^{tetr} = \begin{pmatrix} \gamma & 0 & 0 \\ 0 & \gamma & 0 \\ 0 & 0 & 0 \end{pmatrix} \tag{15c}$$

$$\hat{\epsilon}_4^{tetr} = \begin{pmatrix} \gamma & 0 & 0 \\ 0 & 0 & 0 \\ 0 & 0 & \gamma \end{pmatrix} \tag{15d}$$

$$\hat{\epsilon}_5^{tetr} = \begin{pmatrix} 0 & 0 & 0 \\ 0 & 0 & \gamma \\ 0 & \gamma & 0 \end{pmatrix} \tag{15e}$$

$$\hat{\epsilon}_6^{tetr} = \begin{pmatrix} 0 & \gamma & 0 \\ \gamma & 0 & 0 \\ 0 & 0 & 0 \end{pmatrix} . \tag{15f}$$

The applied strains states do not exactly correspond to the cubic case shown in equation 7. No difference was seen in the elastic constants of a cubic material when using equations 15 or 7. Applying these six strain states separately results in a system of equations involving the elastic constants. The resulting six elastic constants describing a BCT lattice are defined in equation 16 in terms of the pressure and the the second derivative of the energy with respect to γ as

$$\tilde{C}_{11}^{tetr} = \frac{1}{V}\frac{\partial^2 E(V,\hat{\boldsymbol{\epsilon}}_1^{tetr})}{\partial\gamma^2}|_{\gamma=0} \tag{16a}$$

$$\tilde{C}_{12}^{tetr} = P - \frac{1}{V}\frac{\partial^2 E(V,\hat{\boldsymbol{\epsilon}}_1^{tetr})}{\partial\gamma^2}|_{\gamma=0} + \frac{1}{V}\frac{\partial^2 E(V,\hat{\boldsymbol{\epsilon}}_3^{tetr})}{\partial\gamma^2}|_{\gamma=0} \tag{16b}$$

$$\tilde{C}_{13}^{tetr} = P - \frac{1}{2V}\frac{\partial^2 E(V,\hat{\boldsymbol{\epsilon}}_1^{tetr})}{\partial\gamma^2}|_{\gamma=0} - \frac{1}{2V}\frac{\partial^2 E(V,\hat{\boldsymbol{\epsilon}}_2^{tetr})}{\partial\gamma^2}|_{\gamma=0} + \frac{1}{2V}\frac{\partial^2 E(V,\hat{\boldsymbol{\epsilon}}_4^{tetr})}{\partial\gamma^2}|_{\gamma=0} \tag{16c}$$

$$\tilde{C}_{33}^{tetr} = \frac{1}{V}\frac{\partial^2 E(V,\hat{\boldsymbol{\epsilon}}_2^{tetr})}{\partial\gamma^2}|_{\gamma=0} \tag{16d}$$

$$\tilde{C}_{44}^{tetr} = -\frac{P}{2} + \frac{1}{V}\frac{\partial^2 E(V,\hat{\boldsymbol{\epsilon}}_5^{tetr})}{\partial\gamma^2}|_{\gamma=0} \tag{16e}$$

$$\tilde{C}_{66}^{tetr} = -\frac{P}{2} + \frac{1}{V}\frac{\partial^2 E(V,\hat{\boldsymbol{\epsilon}}_6^{tetr})}{\partial\gamma^2}|_{\gamma=0}. \tag{16f}$$

---

[1] T. Saito, T. Furuta, J. Hwang, S. Kuramoto, K. Nishino, N. Suzuki, R. Chen, A. Yamado, K. Ito, Y. Seno, T. Nonaka, H. Ikehata, N. Nagasako, C. Iwamoto, and T. Sakuma, Science, **30**, 464 (2003).

[2] G. I. Taylor, Proc. Roy. Soc. **A145**, 362 (1934).

[3] M. Polyani, Z. Phys. **89**, 363 (1934).

[4] E. Orowan, Z. Phys. **89**, 605 (1934).

[5] T. Li, J. W. Morris, Jr., N. Nagasako, S. Kuramoto, and D. C. Chrzan, PRL **98**, 105503 (2007).

[6] D. C. Chrzan, M. P. Sherburne, Y. Hanlumyuang, T. Li, and J. W. Morris, Jr., Phys. Rev. B **82**, 184202 (2010).

[7] C. A. Sawyer, J. W. Morris, Jr., and D. C. Chrzan, Phys. Rev. B **87**, 134106 (2013).

[8] H. Ikehata, N. Nagasako, T. Furuta, A. Fukumoto, K. Miwa, T. Saito, Phys. Rev. B **70**, 174113 (2004).

[9] S. Kuramoto, T. Furuta, N. Nagasako, and Z. Horita App. Phys. Lett. **95**, 211901 (2009).

[10] A. K. McMahan and J. A. Moriarty, Phys. Rev. B **27**, 3235 (1983).

[11] G. Kresse and J. Hafner Phys. Rev. B **47**, 558 (1993).

[12] G. Kresse and J. Furthmüller, Phys. Rev. B **54**, 11169 (1996).

[13] J. W. Morris, Jr. and C. Krenn, Philos. Mag. A **80**, 2827 (2000).

[14] http://elk.sourceforge.net/

[15] J. P. Perdew, K. Burke and M. Ernzerhof, PRL **77**, 3865 (1996).

[16] G. V. Sin'ko and N. A. Smirnov, Phys. Rev. B **80**, 104113 (2009).

[17] L. J. Slutsky and C. W. Garland, Phys. Rev. **107**, 972 (1957).

[18] G. V. Sin'ko, Phys. Rev. B **77**, 104118 (2008).

[19] H. Olijnyk and W. B. Holzapfel, Phys. Rev. B **31**, 4682 (1985).

[20] T. Tsuchiya and K. Kawamura, J. Chem. Phys. **114**, 10086 (2001).

[21] D. Roundy, C. Krenn, M. Cohen, and J. W. Morris, Jr., Philos. Mag. A **81**, 1725 (2001).

[22] W. Luo, D. Roundy, M. L. Cohen, and J. W. Morris, Jr., Phys. Rev. B **66**, 094110 (2002).

[23] D. C. Wallace, *Thermodynamics of Crystals*, (Wiley, New York, New York 1972).

[24] F. Milstein and S. Chantasiriwan, Phys. Rev. B **58**, 6006 (1998).

[25] M. Šob, L. G. Wang, and V. Vitek, Mater. Sci. Eng. A, **234-236**, 1075 (1997).

[26] N. Nagasako, M. Jahnátek, R. Asahi, J. Hafner, Phys. Rev. B **81**, 094108 (2010).

[27] A. Landa, J. Klepeis, P. Söderlind, I. Naumov, O. Velikokhatnyi, L. Vitos, and A. Ruban, J. Phys.: Condens. Matter 18, 5079 (2006).

[28] M. I. Katsnelson, I. I. Naumov, and A. V. Trefilov, Phase Transitions **49**:1-3, 143 (1994).

[29] L. Qi and D. C. Chrzan, PRL **112**, 115503 (2014).

[30] C. S. Hartley and Y. Mishin, Acta Mater. **53**, 1313 (2005).

[31] C. S. Hartley and Y. Mishin, Mater. Sci & Eng. A **400**, 18 (2005).

[32] N. Lehto and S. Öberg, PRL **80**, 5568 (1998).

[33] V. Vitek, R. C. Perrin, and D. K. Bowen, Philos. Mag. **21**, 1049 (1970).

[34] W. G. Burgers, Physica **1**, 561 (1934).

[35] Y. Hanlumyuang, R. P. Sankaran, M. P. Sherburne, J. W. Morris, Jr., and D. C. Chrzan, Phys. Rev. B **85**, 144108 (2012).

[36] I. S. Winter, S. Chen, and D. C. Chrzan (unpublished).

[37] M. S. Daw, Comput. Mater. Sci. **38**, 293 (2006).

[38] P. Lazar, M. Jahnátek, J. Hafner, N. Nagasako, R. Asahi, C. Blaas-Schenner, M. Stöhr, and R. Podloucky Phys. Rev. B **84**, 054202 (2011).

[39] R. J. Talling, R. J. Dashwood, M. Jackson, S. Kuramoto, D. Dye Scr. Mater. **60**, 1000 (2009).

[40] A. Stukowski, Modelling Simul. Mater. Sci. Eng. **20**, 045021 (2012).

[41] A. Stukowski, Modelling Simul. Mater. Sci. Eng. **18**, 015012 (2010).

[42] M. Y. Gutkin, T. Ishizaki, S. Kuramoto, and I. A. Ovid'ko, Acta Mater. **54**, 2489 (2006).

[43] C. J. Bradley and A. P. Cracknell, *The Mathematical Theory of Symmetry in Solids*, p. 104-105 (Oxford University Press Oxford 2011).

[44] M. Tinkham, *Group Theory and Quantum Mechanics*, p. 71 (Dover Publications, 1992).

[45] S. F. Pugh, Philos. Mag. **45**, 823 (1954).